Front. Phys. 10, 108102 (2015)
DOI 10.1007/s11467-015-0463-3

REVIEW ARTICLE

Tunable topological quantum states in three- and two-dimensional materials

Ming Yang*, **Xiao-Long Zhang**, **Wu-Ming Liu**†

Beijing National Laboratory for Condensed Matter Physics, Institute of Physics, Chinese Academy of Sciences, Beijing 100190, China

*Corresponding authors. E-mail: *myang@iphy.ac.cn, †wmliu@iphy.ac.cn*

Received November 27, 2014; accepted January 6, 2015

We review our theoretical advances in tunable topological quantum states in three- and two-dimensional materials with strong spin–orbital couplings. In three-dimensional systems, we propose a new tunable topological insulator, bismuth-based skutterudites in which topological insulating states can be induced by external strains. The orbitals involved in the topological band-inversion process are the d- and p-orbitals, unlike typical topological insulators such as Bi_2Se_3 and BiTeI, where only the p-orbitals are involved in the band-inversion process. Owing to the presence of large d-electronic states, the electronic interaction in our proposed topological insulator is much stronger than that in other conventional topological insulators. In two-dimensional systems, we investigated 3d-transition-metal-doped silicene. Using both an analytical model and first-principles Wannier interpolation, we demonstrate that silicene decorated with certain 3d transition metals such as vanadium can sustain a stable quantum anomalous Hall effect. We also predict that the quantum valley Hall effect and electrically tunable topological states could be realized in certain transition-metal-doped silicenes where the energy band inversion occurs. These findings provide realistic materials in which topological states could be arbitrarily controlled.

Keywords first-principles calculations, topological insulator, quantum anomalous Hall effect

PACS numbers 81.05.Zx, 73.43.Nq, 73.20.At

Contents

1 Introduction 1
2 Tunable topological insulator in bismuth-based skutterudite 2
2.1 Crystal structure and optimized lattice parameter 2
2.2 Binding energy calculation, phonon mode analysis, and finite-temperature molecular dynamics simulations 2
2.3 Strain-tunable topological phase and d-p band-inversion topological insulator 4
2.4 Partial-density of states and the d-p orbital dominating property 6
2.5 Experimental protocols 6
3 Tunable quantum anomalous Hall effect and valley hall effect in transition-metal-doped silicene 7
3.1 Adsorption and magnetism analysis 7
3.2 Topological states from Chern number analysis 10
3.3 Verification of quantum anomalous Hall effect in 3d-transition-metal-doped silicene 12
4 Conclusions 13
Acknowledgements 13
References and notes 13

1 Introduction

Topological insulators (TIs) are novel quantum states of matter characterized by a bulk gap and gapless edge or surface states, which are protected by time-reversal symmetry [1–13]. The study of three-dimensional (3D) TIs has become one of the most active areas of research in condensed matter physics. Their striking properties lie in the robust surface states that are observed by angle-resolved photoemission spectroscopy. Moreover, TI has become the origin of a number of interesting quantum phenomena such as the quantum anomalous Hall effect [14–22], Majorana fermions [23, 24], and the topological magnetoelectric effect [4].

In two-dimensional (2D) systems, the quantum Hall

© The Author(s) 2015. This article is published with open access at link.springer.com

Frontiers of Physics

effect emerges due to magnetic-field-induced Landau quantization. However, the requirement of an external magnetic field means that it may not be convenient for use in realistic devices. To overcome this inconvenience, researchers proposed the quantum anomalous Hall effect (QAHE) [13] in which the internal magnetism breaks time-reversal symmetry and the spin–orbit coupling (SOC) opens a band gap, resulting in a topologically nontrivial insulating state characterized with the quantized Hall conductivity. Several QAHE materials have been proposed, such as mercury-based quantum wells [14], graphene [15], and transition-metal-doped topological insulators [16, 17, 20, 21]. Recently, the QAHE has been verified experimentally [22].

In this review, we first propose a new tunable topological insulator, bismuth-based skutterudite in which the topological insulating states can be induced by external strains. Then, we demonstrate that silicene decorated with certain 3d transition metals such as vanadium can sustain a stable quantum anomalous Hall effect using both an analytical model and first-principles Wannier interpolation. We also predict the quantum valley Hall effect and electrically tunable topological states could be realized in certain transition-metal-doped silicene. Finally, we summarize our results.

2 Tunable topological insulator in bismuth-based skutterudites

Pressure and strain have been demonstrated as effective methods for tuning the band structures and even topological properties of materials. For instance, $CdSnAs_2$ under a 7% decrease in the lattice constant will become topological insulator [25], while a 6% change in the length of c-axis will drive Bi_2Se_3 from a topological non-trivial phase into a topological trivial phase [26]. Here, we predict a new tunable topological insulator in bismuth-based skutterudites in which the bands involved in the topological band-inversion process are d- and p-orbitals. This band involvement is distinct from that in conventional topological insulators; for instance, in Bi_2Se_3 and BiTeI, the bands involved in the topological band-inversion process are only p-orbitals. Due to the presence of large d-electronic states, the electronic interaction in this topological insulator is much stronger than that in other conventional topological insulators. The stability of this new material is verified by binding energy calculation, phonon mode analysis, and finite-temperature molecular dynamics simulations. This new material can provide nearly zero-resistivity signal current for devices and is expected to be applied in spintronics devices.

2.1 Crystal structure and optimized lattice parameter

Skutterudites, a class of materials with cage-like crystal structure which have received considerable research interest in recent years, are the origin of several unusual phenomena such as heavy fermion superconductivity [27], exciton-mediated superconducting states [28], and Weyl fermions [29]. To include the strong SOC effects in this system, we investigate skutterudites containing the strong SOC element Bi. In particular, the bismuth-based skutterudite $IrBi_3$ has space group $IM\overline{3}$, and its crystal structure is shown in Fig. 1. There are eight Ir atoms and twenty-four Bi atoms in a unit cell. Each Ir atom is surrounded by six Bi atoms, and each Bi atom has two Ir nearest neighbors [see Fig. 1(a)]. The structure has space inversion symmetry with the inversion center of (1/2,1/2,1/2). The structure belongs to the body-centered lattice type, and its primitive cell [Fig. 1(b)] has half the volume of the unit cell. Figur 1(c) shows the Brillouin zone and high symmetric points with Γ (0,0,0), H (0,1/2,0), N (1/4,1/4,0), and P (1/4,1/4,1/4).

After the structure is fully relaxed [30, 31], the calculated total free energy (solid line) as a function of lattice parameter is shown in Fig. 1(d). We find that the optimized lattice parameter of the primitive cell is 8.493 Å, corresponding to the position of free energy minimum. This value is 6% larger than the experimental lattice parameter of $IrSb_3$ [32], which is realistic considering that the Bi atom has a larger atomic radius than the Sb atom.

2.2 Binding energy calculation, phonon mode analysis, and finite-temperature molecular dynamics simulations

To verify the stability of the new material, we perform binding energy calculations, phonon mode analysis, and finite-temperature molecular dynamics (FTMD) simulations. The binding energy is calculated by

$$E_b = E_{\mathrm{IrBi_3}} - n_{\mathrm{Ir}} \cdot E_{\mathrm{Ir}} - n_{\mathrm{Bi}} \cdot E_{\mathrm{Bi}}, \tag{1}$$

where $E_{\mathrm{IrBi_3}}$ denotes the free energy of $IrBi_3$ per primitive cell, E_{Ir} and E_{Bi} are the free energy of crystalline Ir and Bi per atom, respectively, while n_{Ir} and n_{Bi} are the number of Ir and Bi atoms in the $IrBi_3$ primitive cell, respectively. By simple calculation [33], E_b is found to be equal to −3.65 eV per primitive cell. The negative value of the binding energy suggests a stable state of $IrBi_3$.

The phonon dispersion and phonon density of states (DOS) for $IrBi_3$ at zero strain is shown in Fig. 2. In the phonon DOS subfigure, the black solid line corresponds

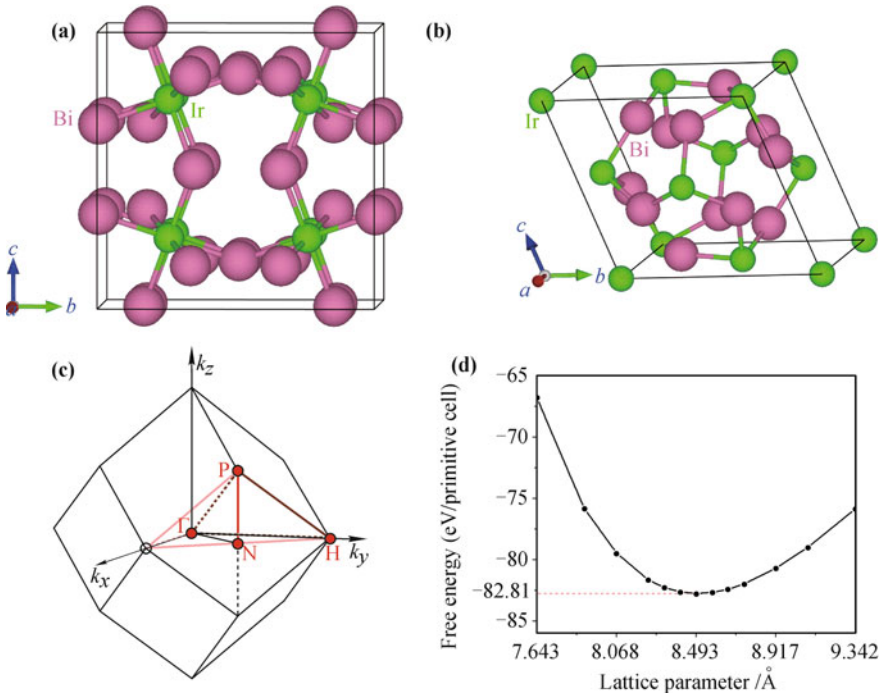

Fig. 1 Crystal structure and Brillouin zone. **(a)** Unit cell of $IrBi_3$, including 8 Ir atoms (*green*) and 24 Bi atoms (*pink*). Each Ir atom is surrounded by 6 Bi atoms and each Bi atom has 2 Ir nearest neighbors. **(b)** The equivalent primitive cell of $IrBi_3$, containing 4 Ir (*green*) atoms and 12 Bi atoms (*pink*). **(c)** The corresponding Brillouin zone and high symmetric points with Γ (0,0,0), H (0,1/2,0), N (1/4,1/4,0) and P (1/4,1/4,1/4). **(d)** Free energy as a function of lattice constant. Reproduced from Ref. [6], Copyright © 2014 Nature Publishing Group.

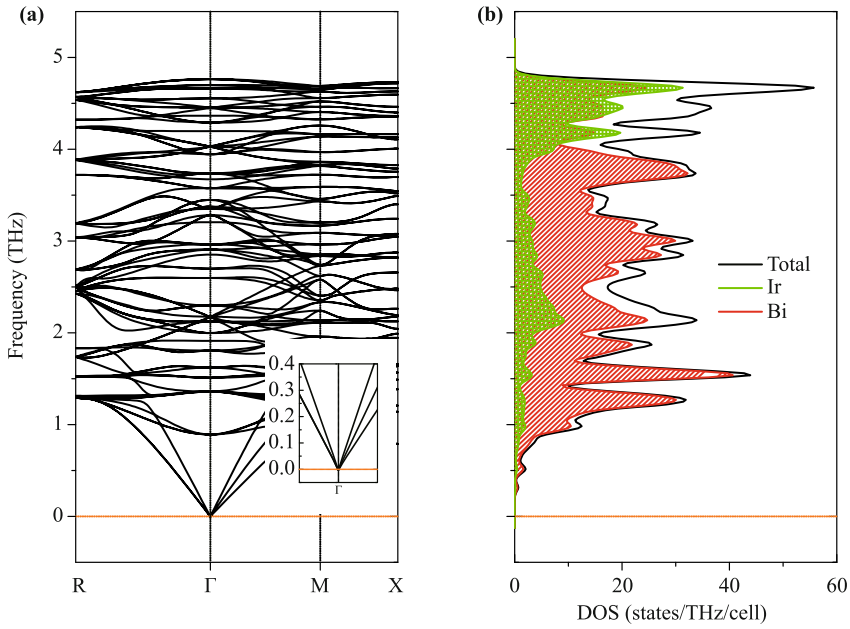

Fig. 2 Phonon dispersion and phonon density of states for $IrBi_3$. Orange dotted lines in all subfigures denote the zero frequency. Calculations are performed at zero strain. **(a)** Phonon dispersion curves for $IrBi_3$, in which the inset shows the dispersion near the zero energy. **(b)** Phonon density of states for $IrBi_3$, in which black solid line represents the total phonon density of states, while the green and red shaded areas represent the states coming from Ir and Bi atoms, respectively. Phonon states in the low energy range are mostly composed of states of Bi atoms, indicating that Bi atoms in $IrBi_3$ are much easier to vibrate than the Ir atoms. The phonon dispersion and phonon density of states shows no imaginary frequency, indicating that $IrBi_3$ is stable. Reproduced from Ref. [6], Copyright © 2014 Nature Publishing Group.

to the total phonon density of states, while the green and red shaded areas correspond to the states of the Ir and Bi atoms, respectively. The phonon states in the low energy range are mostly composed of states from Bi atoms, indicating that Bi atoms in $IrBi_3$ vibrate more easily than Ir atoms. The phonon dispersion and phonon DOS show no imaginary frequencies, indicating that $IrBi_3$ is stable.

To further verify the dynamical stability of the material, we perform finite-temperature molecular dynamics simulations at the temperature of 300 K for room temperature and at 30 K for low temperature. In the simulations, a $2 \times 2 \times 2$ supercell containing 256 atoms is used. The length of the time-step is chosen as 5 fs, and simulations with 1000 steps are executed. We observe that the atoms move the equilibrium positions back and forth, and the extent of such motion under 300 K is larger than that under 30 K. However, no structural collapse occurs throughout the simulations, which can also be observed from the free-energy curves as a function of the time-step as shown in Fig. 3. Moreover, the crystal structure always remains nearly the same as the initial crystal structure. In fact, as shown in the inset of Fig. 3, the crystal structure corresponding to the last free energy maximum in the $T = 300$ K case (right) shows no significant structural differences than the initial crystal structure (left). The lattice relaxation, binding energy calculation, and

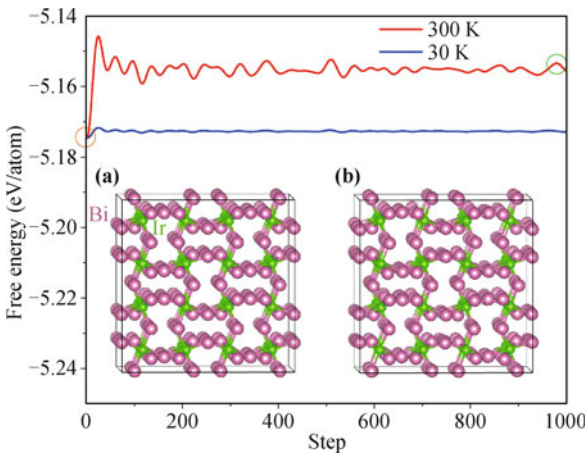

Fig. 3 Finite temperature molecular dynamics. Free energies as functions of time-step at temperature $T = 30$ K (*blue curve*) and $T = 300$ K (*red curve*). The slight shift of the free energy curves corresponds to the oscillations of each atom around their equilibrium position. The absence of sharp changes in such curves indicates that no structural phase-transition happens throughout the whole simulation process. The initial crystal structure (denoted by the orange circle on the free energy curve) is plotted in inset **(a)**. The crystal structure corresponding to the last free energy maximum (denoted by the green circle on the free energy curve) is shown in inset **(b)** as a comparison. It can be seen that, the latter still shows no significant structural differences as compared with the initial crystal structure. Reproduced from Ref. [6], Copyright © 2014 Nature Publishing Group.

phonon mode analysis together with the FTMD simulations provide an authentic test for the stability of the bismuth-based skutterudite $IrBi_3$.

2.3 Strain-tunable topological phase and d-p band-inversion topological insulator

Figure 4 shows the band structures, where the black and blue lines represent the generalized gradient approximation (GGA) and GGA+U band structures, respectively. As shown in Fig. 4(a), $IrBi_3$ resides in the normal metal state before exerting pressure with its bands crossing the Fermi level E_F several times. Figures 4(b) to (d) correspond to the band structures at isotropic strains of 3%, 6%, and 9%, respectively. With the increase in the isotropic strain [(a) to (d)], the valence band crosses E_F along H-N and moves downwards, while the DOS at Fermi level decreases gradually. Under a 9% isotropic strain, the bands cross the Fermi level at the Γ point, but not at other points in Brillouin Zone (BZ) [see Fig. 4(d)]. Moreover, the conduction band minimum and valence band maximum degenerate so that the material behaves as a semi-metal that has a zero energy gap, similar to graphene and $CeOs_4As_{12}$ [10]. This degeneracy at Γ is protected by the cubic symmetry of crystal, which cannot be eliminated by small changes of the lattice constant as we have verified. To shift the degeneracy at Γ, we need to break the symmetry. A simple method is to add an anisotropy similar to the method used for $CdSnAs_2$ [25]. Here, we simply impose an additional 2% suppression on the c-axis of the primitive cell without changing the length of a- and b-axis, which imposes an anisotropy on the system. Though the anisotropy does not change the parities of each band, it opens a gap at the Fermi level, shifting the system to the insulating state [see Fig. 4(e)]. Figure 4(f) shows the Ir-d projected band structure near the Fermi level and near the Γ point in which the radii of red circles correspond to the proportion of Ir-d electrons. The localized bands above the Fermi level are primarily contributed by d-orbitals of Ir atoms. Such band-inversion character is further verified by the modified Becke–Johnson (mBJ) potential, which could predict an accurate band gap and band order [34–36]. The highly dispersive band below the Fermi level is primarily due to the p-orbitals of Bi atoms, and it has little weight from the Ir atoms in k-points far away from the Γ point. However, in the vicinity of Γ point, the weight of the Ir atoms in that band increases rapidly and becomes the dominating orbital component, showing an apparent band inversion. To further confirm the topological properties in such conditions, we calculate the Z_2 topological quantum number. After both applying an isotropic strain

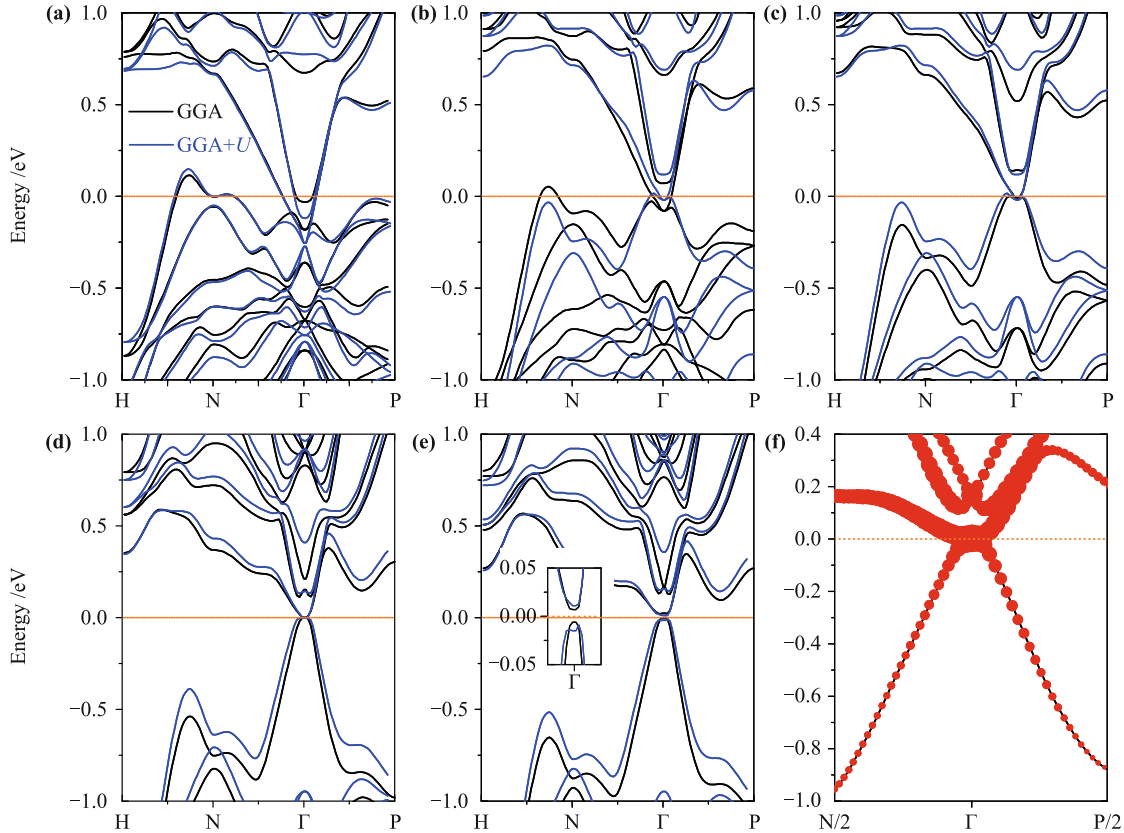

Fig. 4 Band structures of $IrBi_3$. The black and blue lines in all subfigures represent the GGA band structures and GGA+U band structures respectively. **(a)** Band structure without exerting pressure, the system is in normal metal state with its bands go across the Fermi level several times. **(b)**–**(d)** The band structures at isotropic strain 3%, 6%, 9% respectively. With the increase of isotropic strain [(a) to (d)], the valence band crosses the E_F along H-N moves downwards gradually. In the band structure under 9% uniform strain (d), a zero gap metal state is obtained. **(e)** Further imposing a 2% suppression on the length of c-axis of the primitive cell, a gap appeared at the Fermi level due to the breaking of the cubic symmetry. The inset of (e) is the zoom-in of the band structure close to the Fermi level. **(f)** Ir-d projected band structure near Fermi level, the radii of red circles are proportional to the weight of Ir-d states, showing a significant band inversion. Reproduced from Ref. [6], Copyright © 2014 Nature Publishing Group.

Table 1 Parities of top-most isolated valence bands at eight time-reversal invariant momenta. Positive parity is denoted by + while negative denoted by −. Products of the occupied bands at each time-reversal invariant momentum are listed in the right-most column. As is shown, the product of parities of occupied bands contributes a −1 at (0,0,0) while +1 at the seven other time-reversal invariant momenta, resulting in $\nu_0 = 1$, $\nu_1 = \nu_2 = \nu_3 = 0$. Reproduced from Ref. [6], Copyright © 2014 Nature Publishing Group.

TRIM	Parity	Product of the parities
(0,0,0)	++++++++−+−−++++++++−−−+++−−++−+−−+	−
(π,0,0)	−+−+−+−+−++−−+−+−++−−+−+−+−++−−++−+−	+
(0,π,0)	+−+−−++−+−−++−+−+−−++−+−+−+−−++−−+−+	+
(0,0,π)	−+−++−−+−++−−+−+−++−−−++−+−++−−++−+−	+
(π,π,0)	+−+−−++−+−−++−+−+−−++−+−+−+−−++−−+−+	+
(π,0,π)	−+−+−+−+−++−−+−+−++−−+−+−+−++−−++−+−	+
(0,π,π)	+−+−−++−+−−++−+−+−−++−+−+−+−−++−+−−+	+
(π,π,π)	+++++++−++−−+++−++−+−+++−+−−++++−−+−	+

and further applying a uni-axial strain along c-axis, the system still possesses spatial inversion symmetry. Thus, the Fu–Kane method [7] can be utilized to calculate the Z_2 number of our system. The index for strong topological insulators v_0 is expressed as $(-1)^{v_0} = \prod_{i=1}^{8} \delta_i$ in which $\delta_i = \prod_{m=1}^{N} \xi_{2m}(\Gamma_i)$ represents the product of the parities of each occupied band at eight time-reversal invariant momenta Γ_i. The calculated parities of the top-most isolated valence bands (here, referred to as the isolated block of states between –8.0 eV to 0 eV in Fig. 4) at eight time-reversal invariant momenta are listed in Table 1, where the deeper states (those states lower than

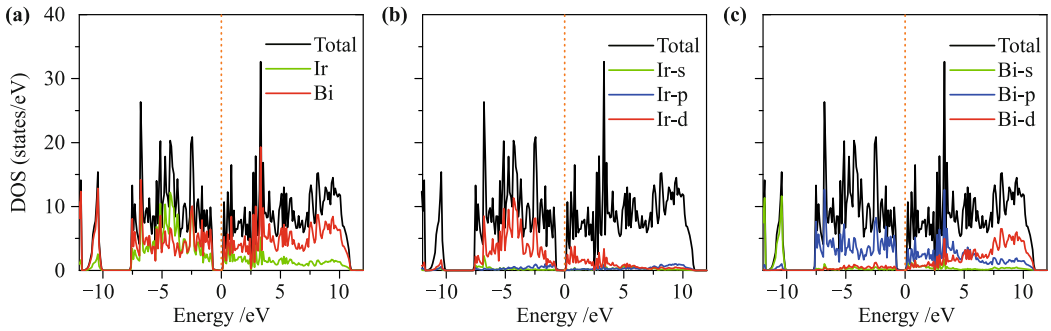

Fig. 5 The atomic- and orbital-resolved density of states. The black solid lines in all subfigures represent the total density of states (DOS). **(a)** Atomic-resolved DOS, in which the green curve represents the states of Ir and the red curve represents the states of Bi. It is clear that both type of atom made a significant contribution to the total DOS, different from MoS_2 where states near Fermi level are dominated by Mo. **(b)** and **(c)** Orbital-resolved DOS of Ir and Bi atom respectively. Green, blue and red curves represent s-, p- and d-orbitals. Reproduced from Ref. [6], Copyright © 2014 Nature Publishing Group.

–9.5 eV in Fig. 5) that were separated far from top-most isolated valence bands are ignored because they do not change the system band topology. As shown, the product of the parities of occupied bands contributes -1 at Γ and contributes $+1$ at the seven other time-reversal invariant momenta. As a result, the Z_2 quantum number is $\nu_0 = 1$, $\nu_1 = \nu_2 = \nu_3 = 0$, which corresponds to a strong topological insulator.

2.4 Partial-density of states and the d-p orbital dominating property

Figure 5 depicts the atomic- and orbital-resolved DOS. The black solid lines in Figs. 5(a)–(c) represent the total DOS. Figure 5(a) shows the atomic-resolved DOS in which the green curve represents the states of Ir and the red curve represents the states of Bi. The DOS of both types of atoms is clearly large, indicating that both types of atoms make a significant contribution to the total DOS. Figures 5(b) and (c) show the orbital-resolved DOS of the Ir and Bi atoms, respectively. Green, blue and red curves represent s-, p- and d-orbitals, respectively. One character of the material introduced here is the large proportion of d-states near E_F.

Further, we calculate the projected band structures of the d-orbitals (see Fig. 6) in the local coordinates of the Bi octahedral. The orange, violet, red, green, and blue colors in Fig. 6 represent the d_{z^2}, $d_{x^2-y^2}$, d_{xy}, d_{yz}, and d_{xz} orbitals, respectively. The radii of the circles are proportional to the weights of corresponding orbitals. The t_{2g} orbitals (including the d_{xy}, d_{yz}, and d_{xz} orbitals) reside far below the Fermi level and are fully occupied. On the other hand, the lowest three conduction bands are primarily contributed by the e_g orbitals (including the d_{z^2} and $d_{x^2-y^2}$ orbitals). More specifically, the $d_{x^2-y^2}$ orbital makes an even larger contribution than the d_{z^2} orbital for the lowest conduction band. The large proportion of d-states near E_F is distinctively different from conventional TI materials. For example, states near E_F primarily contain s-p electrons in HgTe and p-electrons in Bi_2Se_3. The large proportion of d-states near E_F indicates that the electrons in the proposed material process strong electronic correlations and are more localized [37–45] than those in other TI materials. These strong electronic correlations make this material a useful platform for investigating the effect of correlations on the topology as well as a candidate for realizing quantum information devices based on correlations. The localization will enhance the effective mass of bulk electrons, and hence reduce the bulk contribution to the local current at finite temperatures, enhancing the spin-binding property, which is helpful for fabricating spintronics devices with higher stability.

2.5 Experimental protocols

The new strain-induced topological insulator $IrBi_3$ could be grown using the Bridgman method, which has been successfully used for synthesizing the similar materials CoP_3 [46] and $RuSb_3$ [47]. The crystal growth should be conducted in a sealed quartz ampoule. The iridium and bismuth should be coated by graphite and then introduced into the quartz ampoule. Similar to the case of $RhSb_3$ [48], a temperature gradient of about 50°C/cm should be maintained at the growth interface. To remove the excess bismuth in the as-grown crystal, post-annealing should be performed [49]. After the synthesis, the crystal structure of the new material could be characterized by X-ray diffraction using monochromatic Cu Kα radiation [50]. Then, the strains could be generated by a pair of diamond anvils [51], which could generate strong pressure above 200 GPa [52]. Moreover, to detect the real-time pressure strength, the ruby fluorescence method [51, 53] could be utilized. To verify the

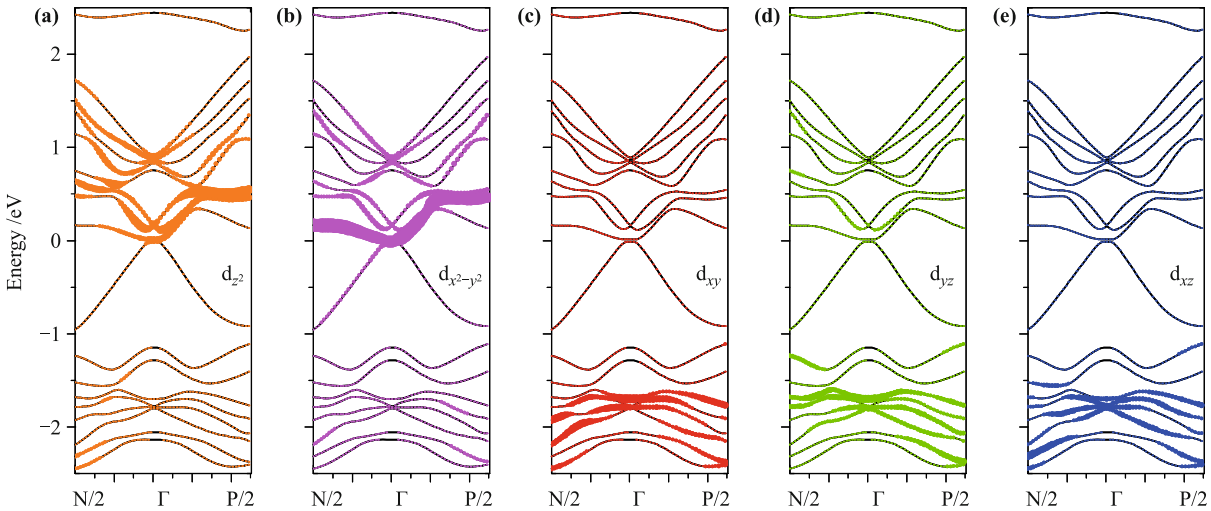

Fig. 6 Orbital-projected band structures. The orange, violet, red, green and blue colors in subfigures represent the d_{z^2}, $d_{x^2-y^2}$ and d_{xy}, d_{yz} and d_{xz} orbitals respectively. The radii of circles are proportional to the weights of corresponding orbitals. The Fermi level is set to be zero energy. It can be seen that, the t_{2g} orbitals (including the d_{xy}, d_{yz}, and d_{xz} orbitals) reside far below the Fermi level and are fully occupied. While, the lowest three conduction bands are mainly contributed by the e_g orbitals (including the d_{z^2} and $d_{x^2-y^2}$ orbitals). More specifically, the $d_{x^2-y^2}$ orbital makes an even larger contribution than the d_{z^2} orbital for the lowest conduction band. Reproduced from Ref. [6], Copyright © 2014 Nature Publishing Group.

topological property of the material, angle-resolved photoemission spectroscopy (ARPES) measurements [9] or the transport measurements [54, 55] could be performed. Similar to Bi_2Se_3, the observation of the spin-Hall current [56] and the non-equally spaced Landau levels [57] in $IrBi_3$ will be signatures of the Dirac fermions in the surface of the topological insulator [1].

3 Tunable quantum anomalous Hall effect and valley Hall effect in transition-metal-doped silicene

For considering the tunable topological topological states in 2D systems, we take transition-metal-doped silicene as an example. Silicene is closely analogous to graphene [58–60] in the sense that it consists of a single layer of Si atoms arranged in a low buckled honeycomb lattice. Moreover, its low energy physics can be described by Dirac-type energy-momentum dispersion akin to that in graphene [61]. Therefore, silicene inherits many intriguing properties such as the expected Dirac fermions and quantum spin Hall effect [11]. The additional buckling degree in the silicene monolayer results in a relatively large (1.55 meV) SOC-induced gap [11], which is absent in graphene. A number of recently reported unusual quantum phenomena [62–66] together with its natural compatibility with the current silicon-based microelectronics industry make silicene a promising candidate for future nano-electronics applications. In this regard, it is highly valuable if magnetism or a sizable band gap or both can be established in nonmagnetic silicene for realizing QAHE with dissipation-less edge states protected by topology.

In this section, we introduce the underlying topological nontrivial states of silicene via systematic investigation of the adsorption of 3d transition metals (TMs). We demonstrate that 3d TMs strongly bonded with silicene and that TM-silicene systems are strongly magnetic. With the combination of tight-binding (TB) model analysis and first-principles Wannier interpolation, show that the vanadium-doped silicene hosts a stable QAHE that survives the strong correlation effects of the adatom. This system can also be half-metallic [67] if the Fermi level is properly tuned. Further, a close study of the TB model in the band-inverted regime gives rise to another topologically nontrivial state, which supports the quantum valley Hall effect (QVHE) [68]. We predict that the resulting QAHE and QVHE can be tuned directly using an external electrical field, which is rather appealing for future nanoelectronics and spintronics applications.

3.1 Adsorption and magnetism analysis

We use a 4×4 supercell of silicene to model the interaction between 3d TMs (Sc, Ti, V, Cr, Mn, Fe, Co, Ni) and silicene. Because silicene has a buckled geometry, we consider three high symmetry adsorption sites, namely the hollow (H) site at the center of a hexagon and two top sites denoted as T_A and T_B, corresponding to the top Si atoms belonging to the A and B sublattice, respectively (see Fig. 7). The simulations have been performed

separately within the GGA [69] and GGA+U [71, 72] framework to evaluate the effect of on-site Coulomb interactions among the 3d electrons of the adatoms on the equilibrium structure and the magnetic properties of the TM-silicene system, respectively.

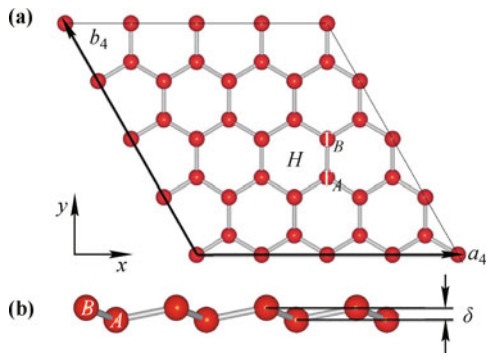

Fig. 7 The lattice geometry of 3d transition metals doped silicene. The lattice geometry of 3d transition metals doped silicene with lattice constant $|a_4| = |b_4| = 4a$, where $a = 3.86$ Å is the lattice constant of silicene. **(a)** Top view of 4×4 silicene monolayer where the 3 adsorption sites [Hollow (H), top of A sublattice (T_A) and B sublattice (T_B)] are marked out with black letters. **(b)** Side view of silicene, the two equivalent Si sublattices are labeled as A and B, respectively, with a buckled distance $\delta = 0.44$ Å. Reproduced from Ref. [17], Copyright © 2013 Nature Publishing Group.

We first focus on the GGA case. Of the three adsorption sites, all 3d TMs energetically favor the H site, which is 0.02 eV –0.60 eV and 0.20 eV–0.80 eV higher in adsorption energy than the T_A and T_B site, respectively. Here, $\Delta E = E_s + E_{ads} - E_{s-ads}$ is the adsorption energy within GGA, and E_s, E_{ads}, and E_{s-ads} represent the energies of the 4×4 pristine silicene, single adatom, and silicene-adatom system, respectively. The bonding between 3d TMs and silicene is strongly covalent as manifested by a much larger ΔE ranging from 2.44 eV to 4.75 eV. The unusual large ΔE compared with that in graphene [73, 74] could be related to the covalently more active sp^3-like orbitals of silicene, which are a result of the unique buckled geometry.

Most TM-doped silicenes exhibit magnetism with sizable magnetic moments ranging from $\sim 1\ \mu_B$ to $\sim 5\ \mu_B$, with the exception of Ni-doped silicene, which is similar to the graphene case [73, 74]. A relatively large magnetic moment is key to the realization of QAHE in silicene, which we discuss later. We also note that when some TMs (Sc, Ti, Cr) adsorb on the H site, the DOS show peaks at the Fermi level, indicating that these systems could be magnetically unstable and may undergo Jahn–Teller distortion to lower total energy. In the case of Sc-silicene, we artificially move one of three Si atoms nearest to Sc to break the C_3 rotational symmetry. After relaxation, the three nearest Si atoms to Sc, which originally arranged themselves as a coplanar, regular triangle (bond length $d_{\mathrm{Si-Sc}}$ equal to 2.62 Å) is now distorted to an isosceles triangle ($d_{\mathrm{Si-Sc}}$ with bond lengths of 2.63 Å, 2.63 Å, and 3.12 Å) by pushing an Si atom away from the upper sublattice plane by 1.24 Å. The distorted Sc-silicene system becomes more stable than C_{3v} symmetric system because the total energy is lowered by 0.1 eV. Similar to the Sc-doped silicene case, we could expect the Jahn–Teller distortion to further stabilize the Ti-silicene and Cr-silicene systems; nevertheless, the distortion for these two systems was rather weak.

The resulting magnetic moments and possible aforementioned Jahn–Teller distortion can be understood by symmetry considerations. When TMs are deposited on high symmetry sites of silicene (H, T_A, T_B), the 3d subshell of the adatom splits into three groups under the C_{3v} symmetric crystal field of system: the $3d_{3z^2-r^2}$ state corresponding to the A_1 symmetry group, the twofold degenerate E_1 group consisting of the $3d_{xz}$ and $3d_{yz}$ states, and the E_2 group consisting of the $3d_{xy}$ and $3d_{x^2-y^2}$ states. Therefore, the three groups of 3d states hybridize with the π orbitals of silicene weakly or strongly according to the different symmetrical properties in similar way as that in benzene [75] and graphene [76]. Because 3d orbitals are anti-bonding states, the energy order of the orbitals are usually $\epsilon(E_2) < \epsilon(A_1) < \epsilon(E_1)$. In general, $\epsilon(E_2)$ and $\epsilon(A_1)$ are close to each other due to their similar hybridization strength with π orbitals. After incorporating spin polarization, the three groups of states split, according to different splitting energy, into 10 spin-polarized orbitals. Meanwhile, the outer 4s electrons of the adatoms experience relatively large electrostatic interaction from the π manifold of silicene, compared to that from the 3d shells, due to the spherical symmetry and delocalized nature of the π manifold, which enables charge transfer from the 4s to 3d shells. Thus, the crystal field splitting and spin splitting, together with the occupation number, primarily dominate the electronic structure of adsorbed TM ions.

The spin splitting for Sc in Sc-doped silicene is around 0.2 eV, which is smaller than ligand field splitting between E_2 and A_1. In total, there are three electrons occupying 3d orbitals (see Fig. 8). As a result, two of these three electrons occupy the majority E_2 orbitals, while the remaining electron occupies the doubly degenerate minority E_2 orbitals, leading to 1 μ_B magnetic moment and potential Jahn–Teller distortion. Owing to the relatively large splitting of A_1 (1 eV), the majority A_1 orbital in Ti-doped silicene is occupied before the doubly degenerate minority E_2 orbitals as indicated in the inset of Fig. 8, showing the projected density of states (PDOS) of Ti from GGA calculations. This leads to the peaks at the

Fermi level and the magnetic moment of 2 μ_B. For V, the spin splitting is much larger, and a high spin state with 5 μ_B moment state is realized, which is essential to the realization of QAHE in silicene. The other cases can be understood with similar arguments.

Considering that the strong correlation effect of 3d electrons apparently affect the description of adsorption, we consider the GGA+U case. After ionic relaxation, the adsorption geometry of the adatom-silicene system strongly changed compared with GGA case. Moreover,

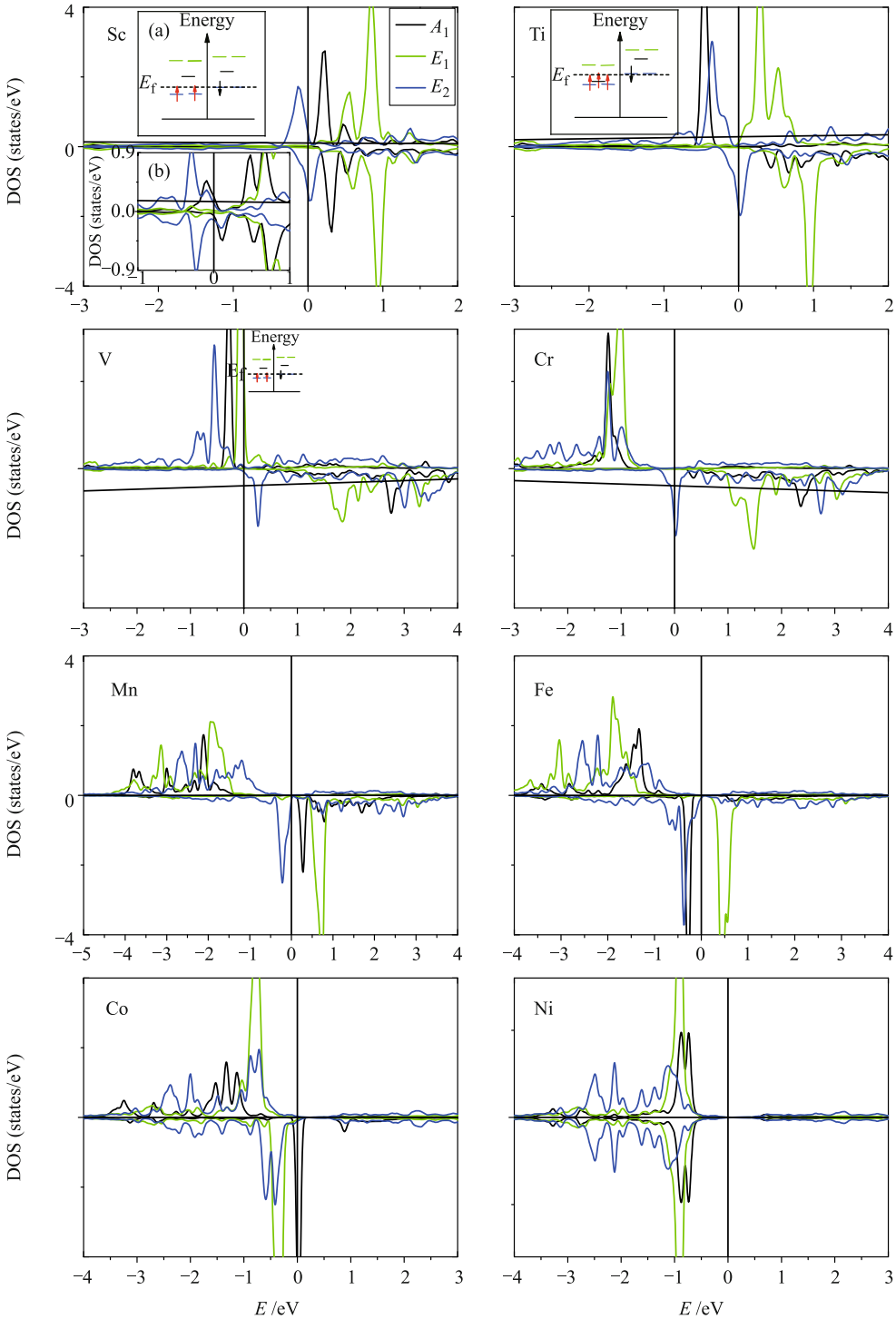

Fig. 8 Projected density of states. Projected density of states (PDOS) of all 3d transition metals adsorbed on the stable site (Hollow) of monolayer silicene from generalized gradient approximation (GGA), where positive (negative) values are for majority (minority) spin. The inset (b) in Sc indicates the Jahn–Teller distorted PDOS. The Fermi energy is set to 0 eV. Reproduced from Ref. [17], Copyright © 2013 Nature Publishing Group.

most 3d TMs still favor the H site (except for Mn, which now energetically favors the T_A site). The geometry change of the adatom-silicene systems is a direct consequence of the on-site Coulomb interactions among 3d electrons, which modify the electron distribution in 3d and 4s shells of adatoms and π orbitals of silicene as shown from the changes in the magnetic moment.

3.2 Topological states from Chern number analysis

In this section, we review the QAHE in the absence of external field via doping with 3d TMs and predict the electrically tunable topological states. As shown in Refs. [74, 77], the QAHE could be realized via doping certain 3d or 5d adatoms on the hollow site of graphene. In Fe-doped graphene [74], the QAHE gaps occur around the Dirac K points of the Brillouin zone, and the low-energy physics can be described by a Hamiltonian for graphene in the presence of the extrinsic Rashba SOC (λ_R^{ext}) and exchange field (M) [78], introduced solely by the adatom. However, in silicene, when depositing 3d TMs on the stable adsorption site or when applying a perpendicular external electric field, the induced inequality of the AB sublattice potential (Δ) necessarily occurs and competes with the magnetization [62, 63]. Furthermore, the QAHE in silicene lives only in certain ranges of parameter space [62]. Moreover, owing to the low buckled structure, there exists so-called intrinsic Rashba SOC (λ_R^{int}) [70]. The interplay between the two types of Rashba SOC (λ_R^{ext} and λ_R^{int}) will lead to an electrically tunable topological phase transition, as we will demonstrate later. Below, we identify conditions for the realization of QAHE in silicene based on an effective Hamiltonian [70] by introducing a staggered AB sublattice potential in addition to SOC (λ_R^{ext} and λ_{so}) and the exchange field (M), which is similar to the one used in Ref. [62].

The Hamiltonian of this system is $H_{eff}^{\pm} = H_s^{\pm} + H_d^{\pm}$, with $H_s^{\pm} = \varepsilon_{eff}\tau_0 \otimes \sigma_0 \pm \tau_3 \otimes h_{11} + \hbar v_F(k_x\tau_1 \mp k_y\tau_2) \otimes \sigma_0$, $H_d^{\pm} = \lambda_R^{ext}(\pm\tau_1 \otimes \sigma_2 - \tau_2 \otimes \sigma_1) + \Delta\tau_3 \otimes \sigma_0 + M\tau_0 \otimes \sigma_3$, and $h_{11} = -\lambda_{so}\sigma_3 - a\lambda_R^{int}(k_y\sigma_1 - k_x\sigma_2)$. Here, the basis is chosen as $\{A, B\} \otimes \{\uparrow, \downarrow\}$, and $H_{eff}^{\pm}$ are the total Hamiltonians for the two inequivalent Dirac points $K\,(+)$ and $-K\,(-)$. Moreover, $H_s^{\pm}$ are the low-energy effective Hamiltonians for the quantum spin Hall insulator silicene, and $H_d^{\pm}$ include all effects introduced by the 3d dopants, including the effective spin-dependent magnetic field M, site-dependent staggered potential Δ, and the resulting extrinsic Rashba SOC λ_R^{ext}. The Pauli matrices τ and σ act separately on pseudospin (sublattice) and spin space, respectively, ε_{eff} is the $\varepsilon_1 - \lambda_{2nd}$ term in Ref. [11], v_F and a represent the Fermi velocity and the lattice constant, respectively, and λ_{so} stands for the effective SOC.

We can derive the band structures around each valley

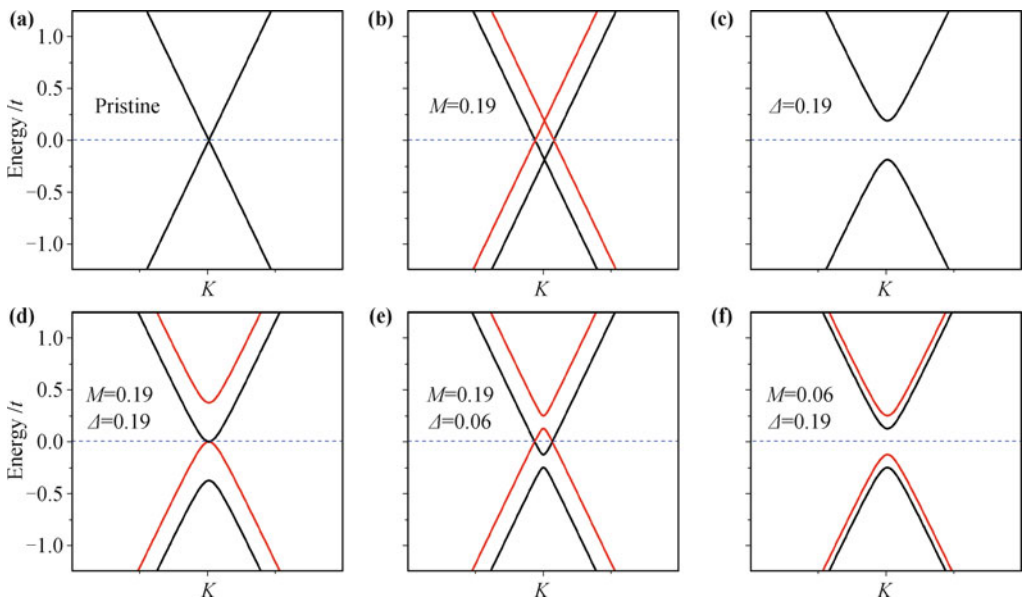

Fig. 9 Evolution of band structure around valley K. The evolution of band structure around valley K from the interplay between exchange field M and staggered potential Δ (in unit of t). The red (black) lines are for the majority (minority) spin. **(a)** The band structure of pristine silicene with perfect Dirac-like energy dispersion. **(b)** The spin degeneracy is lifted when only exchange field M is turned on. **(c)** The system becomes insulating with the valence and conduction bands twofold degenerated when only staggered potential Δ is added. **(d)** When $M = \Delta$, there always exists a degenerate point right at the Fermi level. **(e)** When $M > \Delta$, the two spin subbands near Fermi level cross, resulting a circular Fermi surface. **(f)** When $M < \Delta$, the system enters insulating state. Reproduced from Ref. [17], Copyright © 2013 Nature Publishing Group.

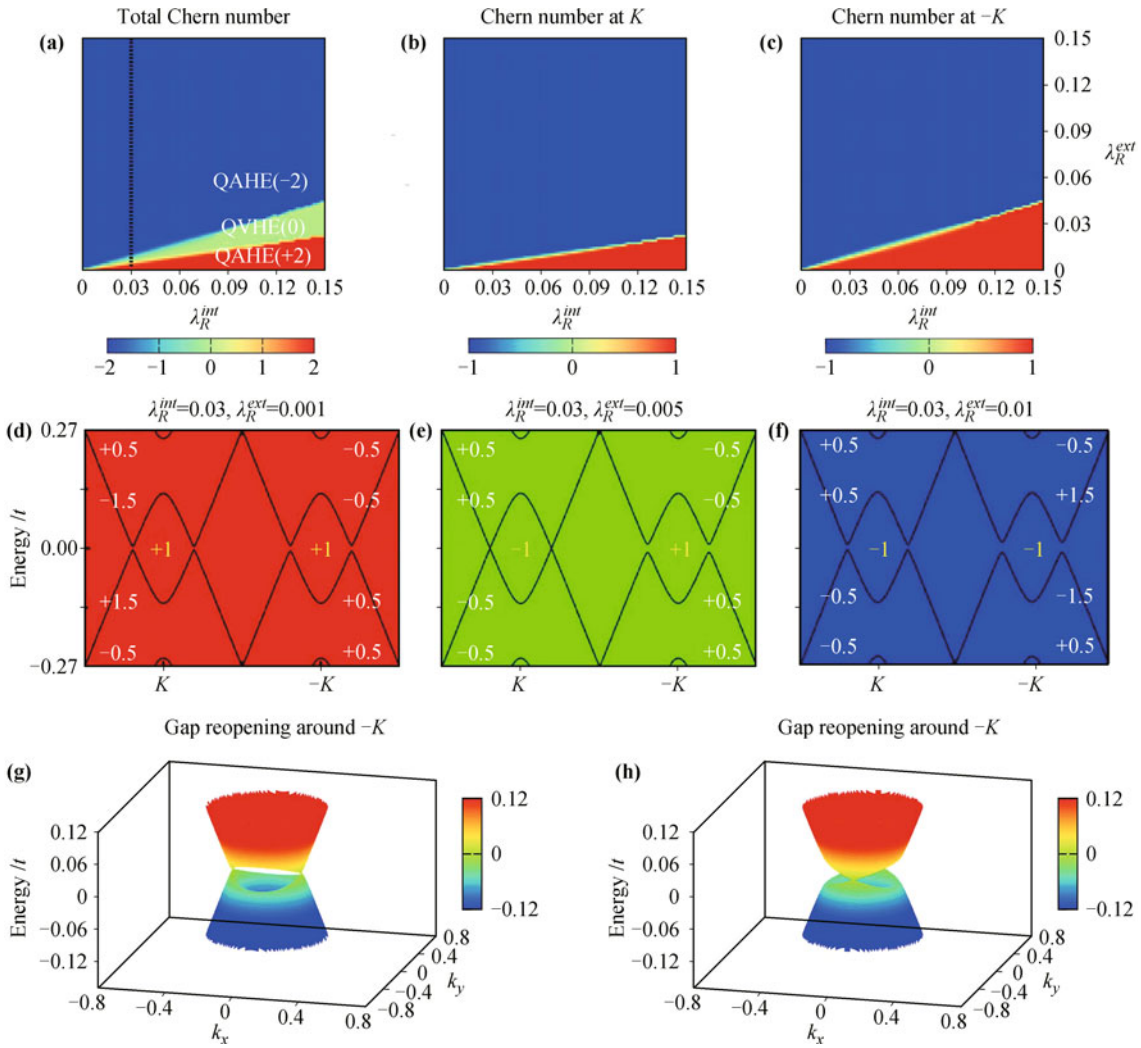

Fig. 10 The transition of Chern number by tuning Rashba SOC. The transition of Chern number by tuning λ_R^{ext} and λ_R^{int} (in unit of t). **(a)** Three topological nontrivial states, QAHE(2), QVHE(0) and QAHE(–2) with Chern number +2, 0, and −2, can be obtained from different combination of λ_R^{ext} and λ_R^{int}. **(b)** and **(c)** represent the the variation of $\mathcal{C}_K$ and $\mathcal{C}_{-K}$. **(d)**, **(e)** and **(f)** depict the band structure along $k_y = 0$ line in BZ for the three topological states (QHE(2), QVHE(0) and QHE(–2)) in (a). The yellow integers (±1) represent $\mathcal{C}_K$ and $\mathcal{C}_{-K}$, corresponding to the sum of topological charge of each valence bands (the white ±0.5 and ±1.5). **(g)** and **(h)** show the gap closing around K and $-K$. They are the transition states from QAHE(+2) to QVHE(0) and from QVHE(0) to QAHE(–2), respectively. Reproduced from Ref. [17], Copyright © 2013 Nature Publishing Group.

(K and $-K$) in the Brillouin zone by diagonalizing the above Hamiltonian. The interplay between the exchange field (M) and staggered potential (Δ) (see Fig. 9) causes the energy bands with opposite spin to intersect, which is essential to the QAHE in Fe-doped graphene when $M/\Delta > 1$. The situation here is different from that in Ref. [78], where $\Delta = 0$ and where two degenerate points always exist around the Dirac point as long as $M \neq 0$.

Either the extrinsic or the intrinsic Rashba SOC would induce an insulating state when starting from the case $M/\Delta > 1$. To identify the topological properties of the resulting insulating state, we perform the Chern number ($\mathcal{C}$) analysis [79], where $\mathcal{C}$ can be obtained by integrating over the first Brillouin zone (BZ): $\mathcal{C} = \frac{1}{2\pi}\int_{BZ}\Omega(\boldsymbol{k})\mathrm{d}^2k$. Here, $\Omega(\boldsymbol{k})$ is the usual Berry curvature of all occupied states [80]:

$$\Omega_z(\boldsymbol{k}) = -2\sum_n\sum_{m\neq n} f_n \mathrm{Im}\frac{\langle\psi_{n\boldsymbol{k}}|v_x|\psi_{m\boldsymbol{k}}\rangle\langle\psi_{m\boldsymbol{k}}|v_y|\psi_{n\boldsymbol{k}}\rangle}{(\epsilon_{m\boldsymbol{k}}-\epsilon_{n\boldsymbol{k}})^2}, \tag{2}$$

where f_n is the Fermi–Dirac distribution function for band n, $\psi_{n\boldsymbol{k}}$ is the Bloch function of the eigenenergy $\epsilon_{n\boldsymbol{k}}$, and v_x and v_y are the velocity operators. The anomalous Hall conductivity is readily given by $\sigma_{xy} = (e^2/h)\mathcal{C}$. Interestingly, the extrinsic Rashba SOC (λ_R^{ext}) gives the insulating state with $\mathcal{C} = +2$, while the intrinsic Rashba SOC (λ_R^{int}) leads to that with $\mathcal{C} = -2$. One may expect

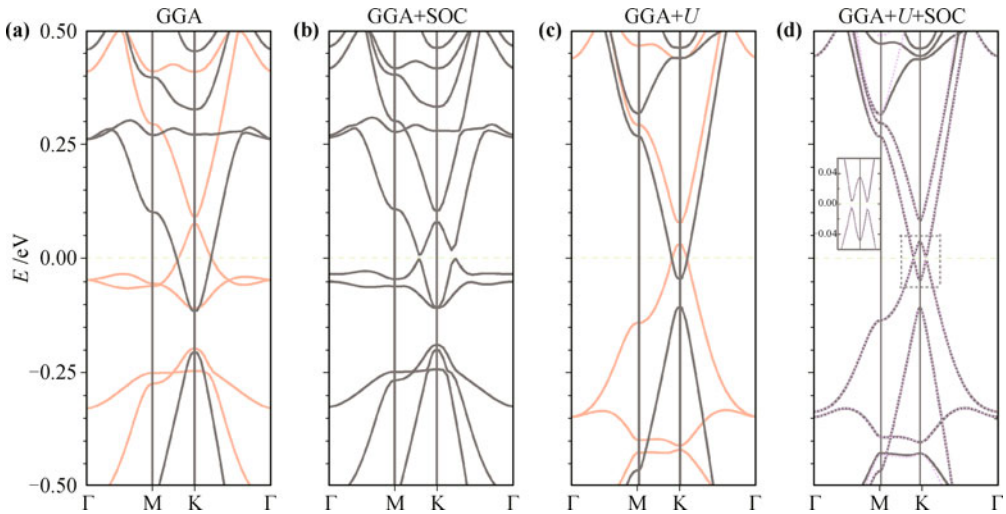

Fig. 11 The band structures of V doped silicene. The band structures of V doped silicene from GGA **(a, b)** and GGA+U **(c, d)**, respectively. The red (black) color in (a) and (c) correspond to majority spin (minority spin) subbands. After including SOC effect, a gap is opened at the Fermi level (b, d). In (d), the band structure from Wannier interpolation is also shown in pink dashed lines. Reproduced from Ref. [17], Copyright © 2013 Nature Publishing Group.

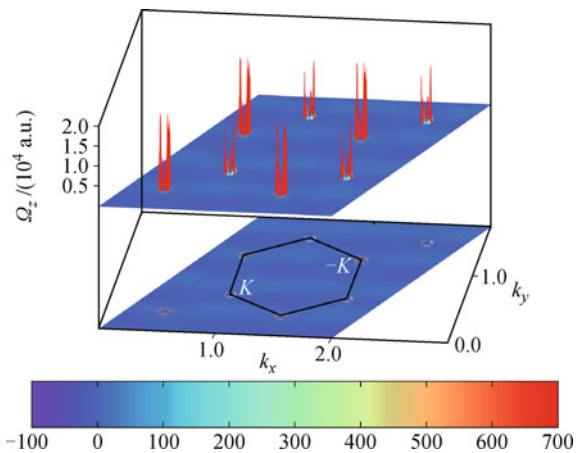

Fig. 12 The Berry curvature distribution of V doped silicene. The distribution of Berry curvature ($\Omega_z(k)$) of all occupied states in V doped silicene from GGA+U+SOC. The first Brillouin zone is marked out with black hexagon. The small red circles in the projection drawing represent the most non-zero values of Berry curvature. Reproduced from Ref. [17], Copyright © 2013 Nature Publishing Group.

that a different Chern number state can be realized by properly tuning the two types of Rashba SOC in experiments. Figure 10(a) indicates that this is indeed the case: $\mathcal{C}$ can take integer values of $+2, 0, -2$ with different combinations of λ_R^{int} and λ_R^{ext}. Careful study shows that the tunable $\mathcal{C}$ originates from the different response of bulk gap to the two types of Rashba SOC (λ_R^{int} and λ_R^{ext}) around K and $-K$. For example, when increasing λ_R^{ext} while keeping λ_R^{int} fixed at $0.03t$ ($t = 1.6$ eV is the nearest neighbor hopping parameter [70]) as shown in Fig. 10(a), we can see clearly the transition of the Chern number of each valley ($\mathcal{C}_K$ and $\mathcal{C}_{-K}$) from $+1$ to -1 at different rates, i.e., $\mathcal{C}_K$ experiences a topological transition earlier than $\mathcal{C}_{-K}$ [see Figs. 10(b) and (c)]. The step change of $\mathcal{C}_K$ and $\mathcal{C}_{-K}$ is justified by the observation of bands touching and gap reopening around each valley [Figs. 10(d) and (f)]. Notice that the rotational symmetry of the effective Hamiltonian along the z-direction in any angle is broken after introducing the Rashba SOC terms. Hence, the band only touches the $k_y = 0$ line in the BZ for valley K [Fig. 10(g)] or the $k_x = 0$ line for valley $-K$ [Fig. 10(h)]. Consequently, the system can be in the QAHE phase (with $\mathcal{C}$ being $+2$ or -2) or the QVHE phase (with $\mathcal{C} = 0$ and $\mathcal{C}_K = -\mathcal{C}_{-K} = -1$) depending on the value of λ_R^{ext}, which is controllable through an external gate voltage.

However, the effective SOC (λ_{so}) further breaks the particle-hole symmetry of the above Hamiltonian, causing the energy bands shift up (at valley K) or down (at valley $-K$) relative to the Fermi level while leaving the topological charge of each valley unchanged. Hence, as long as the shifting is small, the system is still insulating, and the above discussion of topological transition remains valid.

3.3 Verification of quantum anomalous Hall effect in 3d-transition-metal-doped silicene

We now introduce the verification of topologically nontrivial phases using first-principles calculations. As an example, in Ti-, V-, Cr-, or Mn-doped silicene, the opposite spin subbands cross near the Fermi level due to the relatively large magnetization. This behavior closely resembles the band inversion case ($M/\Delta > 1$) in the TB

model above [see Fig. 9(e)]. The spin-up and spin-down subbands near the Fermi level are also gapped [Figs. 11(a) and (c)], which makes these systems candidates for half-metallic materials if the Fermi level is tuned properly. We take V-silicene as a prototype because this system is insulating with an energy gap around 6 meV [Fig. 11(b)] when only the SOC is considered. Moreover, the SOC-induced band gap in V-silicene is stable regardless of the inclusion of the effective U.

As discussed above, the V-silicene system could be in one of three topologically nontrivial states [QAHE(+2), QVHE(0), QAHE(–2)] when only SOC is considered. Thus, we need to obtain an accurate Berry curvature distribution and Chern number at the first-principles level in V-doped silicene [81, 82]. As indicated in Fig. 11(d), the band structure produced by Wannier interpolation is consistent with that from first-principles calculations. In Fig. 12, the Berry curvature [$\Omega_z(k)$] in k-space is explicitly shown. As we may observe, the most nonzero values (positive) of the Berry curvature are distributed near the Dirac K points, forming small circles, where the avoided crossing occurs [Fig. 11(d)]. Moreover, we find that the Chern number of all occupied bands equals an integer value of +2, which indicates that the V-doped silicene is in the QAHE(+2) phase, by the integral over BZ. The tight-binding parameters corresponding to this case [Fig. 11(d)] are estimated as M=75 meV, Δ=21 meV, λ_{so}=5 meV, λ^{int}= 8 meV, and λ^{ext} = 1.5 meV. Note that, here, λ^{ext} is induced solely by vanadium adatom.

To introduce the topological phase transition in the V-silicene system, we can apply an additional external electric field to increase λ_R^{ext}. According to the phase diagram presented in Fig. 10, we can give an estimation of the magnitude of the external electric field. The value of λ_R^{ext} required for the system to enter the QVHE(0) state is about 1.55 meV. Consequently, an extra 0.05 meV λ_R^{ext} should be supplied by an external electric field E_z, which is about (12.5 V)/(300 nm) according to a rough estimation [70]. Further, we need to apply E_z of about (225 V)/(300 nm) to generate an additional 0.9 meV λ_R^{ext} (total λ_R^{ext} is about 2.4 meV) for the system to enter the QAHE(–2) phase.

4 Conclusions

In summary, we have reviewed our recent progress in tunable topological quantum states in three-dimensional and two-dimensional materials with strong spin-orbital couplings. By applying proper strain, we demonstrate the bismuth-based skutterudite could be tuned into a topological insulator with d-p topological band inversion. Moreover, by 3d-transition-metal doping, silicene can sustain the quantum anomalous Hall effect and quantum valley Hall effect. These findings provide evidence for realistic materials in which the topological states could be arbitrarily controlled.

Acknowledgements We acknowledge helpful discussions with H. M. Weng, L. F. Liu, X. X. Wu., C. C. Liu, and J. J. Zhou. This work was supported by the National Key Basic Research Special Foundation of China under grant Nos. 2011CB921502 and 2012CB821305, the National Natural Science Foundation of China under grant Nos. 61227902, 61378017, and 11434015, SKLQOQOD under grant No. KF201403, SPRPCAS under grant No. XDB01020300. The numerical calculations are performed on the Shenteng supercomputer at CNIC-CAS and on the Dawning cluster at IOP-CAS.

Open Access This article is distributed under the terms of the Creative Commons Attribution License which permits any use, distribution, and reproduction in any medium, provided the original author(s) and the source are credited.

References and notes

1. B. A. Bernevig, T. A. Hughes, and S. C. Zhang, Quantum spin Hall effect and topological phase transition in HgTe quantum wells, *Science* 314(5806), 1757 (2006)
2. H. Lin, L. A. Wray, Y. Xia, S. Y. Xu, S. Jia, R. J. Cava, A. Bansil, and M. Z. Hasan, Half-Heusler ternary compounds as new multifunctional experimental platforms for topological quantum phenomena, *Nat. Mater.* 9(7), 546 (2010)
3. S. Chadov, X. L. Qi, J. Kubler, G. H. Fecher, C. Felser, and S. C. Zhang, Tunable multifunctional topological insulators in ternary Heusler compounds, *Nat. Mater.* 9(7), 541 (2010)
4. X. L. Qi, T. L. Hughes, and S. C. Zhang, Topological field theory of time-reversal invariant insulators, *Phys. Rev. B* 78(19), 195424 (2008)
5. H. J. Zhang, C. X. Liu, X. L. Qi, X. Dai, Z. Fang, and S. C. Zhang, Topological insulators in Bi_2Se_3, Bi_2Te_3 and Sb_2Te_3 with a single Dirac cone on the surface, *Nat. Phys.* 5(6), 438 (2009)
6. M. Yang and W. M. Liu, The d-p band-inversion topological insulator in bismuth-based skutterudites, *Scientific Reports* 4, 5153 (2014)
7. L. Fu and C. L. Kane, Topological insulators with inversion symmetry, *Phys. Rev. B* 76(4), 045302 (2007)
8. Y. Xia, D. Qian, D. Hsieh, L. Wray, A. Pal, H. Lin, A. Bansil, D. Grauer, Y. S. Hor, R. J. Cava, and M. Z. Hasan, Observation of a large-gap topological-insulator class with a single Dirac cone on the surface, *Nat. Phys.* 5(6), 398 (2009)
9. Y. L. Chen, Studies on the electronic structures of three-dimensional topological insulators by angle resolved photoemission spectroscopy, *Front. Phys.* 7(2), 175 (2012)
10. B. H. Yan, L. Muchler, X. L. Qi, S. C. Zhang, and C. Felser, Topological insulators in filled skutterudites, *Phys. Rev. B* 85(16), 165125 (2012)

11. C. C. Liu, W. X. Feng, and Y. G. Yao, Quantum spin Hall effect in silicene and two-dimensional germanium, *Phys. Rev. Lett.* 107(7), 076802 (2011)

12. F. D. Sun, X. L. Yu, J. W. Ye, H. Fan, and W. M. Liu, Topological quantum phase transition in synthetic non-abelian gauge potential: Gauge invariance and experimental detections, *Scientific Reports* 3, 2119 (2013)

13. F. D. M. Haldane, Model for a quantum Hall effect without Landau levels: Condensed-matter realization of the "parity anomaly", *Phys. Rev. Lett.* 61(18), 2015 (1988)

14. C. X. Liu, X. L. Qi, X. Dai, Z. Fang, and S. C. Zhang, Quantum anomalous Hall effect in $Hg_{1-y}Mn_yTe$ quantum wells, *Phys. Rev. Lett.* 101(14), 146802 (2008)

15. Z. H. Qiao, W. Tse, H. Jiang, Y. G. Yao, and Q. Niu, Two-dimensional topological insulator state and topological phase transition in bilayer graphene, *Phys. Rev. Lett.* 107(25), 256801 (2011)

16. R. Yu, W. Zhang, H. J. Zhang, S. C. Zhang, X. Dai, and Z. Fang, Quantized anomalous Hall effect in magnetic topological insulators, *Science* 329(5987), 61 (2010)

17. X. L. Zhang, L. F. Liu, and W. M. Liu, Quantum anomalous Hall effect and tunable topological states in 3d transition metals doped silicene, *Scientific Reports* 3, 2908 (2013)

18. Y. Y. Zhang, J. P. Hu, B. A. Bernevig, X. R. Wang, X. C. Xie, and W. M. Liu, Localization and the Kosterlitz–Thouless transition in disordered graphene, *Phys. Rev. Lett.* 102(10), 106401 (2009)

19. R. Y. Liao, Y. X. Yu, and W. M. Liu, Tuning the tricritical point with spin-orbit coupling in polarized fermionic condensates, *Phys. Rev. Lett.* 108(8), 080406 (2012)

20. J. M. Zhang, W. G. Zhu, Y. Zhang, D. Xiao, and Y. G. Yao, Tailoring magnetic doping in the topological insulator Bi_2Se_3, *Phys. Rev. Lett.* 109(26), 266405 (2012)

21. Z. F. Wang, Z. Liu, and F. Liu, Quantum anomalous Hall effect in 2D organic topological insulators, *Phys. Rev. Lett.* 110(19), 196801 (2013)

22. C. Z. Chang, J. Zhang, X. Feng, J. Shen, Z. Zhang, M. Guo, K. Li, Y. Ou, P. Wei, L. L. Wang, Z.Q. Ji, Y. Feng, S. Ji, X. Chen, J. Jia, X. Dai, Z. Fang, S. C. Zhang, K. He, Y. Wang, L. Lu, X. C. Ma, and Q. K. Xue, Experimental observation of the quantum anomalous Hall effect in a magnetic topological insulator, *Science* 340(6129), 167 (2013)

23. L. Fu and C. L. Kane, Superconducting proximity effect and Majorana fermions at the surface of a topological insulator, *Phys. Rev. Lett.* 100(9), 096407 (2008)

24. R. P. Tiwari, U. Zülicke, and U. Bruder, Majorana fermions from Landau quantization in a superconductor and topological-insulator hybrid structure, *Phys. Rev. Lett.* 110(18), 186805 (2013)

25. W. X. Feng, D. Xiao, J. Ding, and Y. G. Yao, Three-dimensional topological insulators in IIII-VI2 and II-IV-V2 chalcopyrite semiconductors, *Phys. Rev. Lett.* 106(1), 016402 (2011)

26. W. L. Liu, X. Peng, C. Tang, L. Sun, K. Zhang, and J. Zhong, Anisotropic interactions and strain-induced topological phase transition in Sb_2Se_3 and Bi_2Se_3, *Phys. Rev. B* 84(24), 245105 (2011)

27. G. Seyfarth, J. Brison, M.A. Méasson, J. Flouquet, K. Izawa, Y. Matsuda, H. Sugawara, and H. Sato, Multiband superconductivity in the heavy fermion compound $PrOs_4Sb_{12}$, *Phys. Rev. Lett.* 95(10), 107004 (2005)

28. M. Matsumoto and M. Koga, Exciton mediated superconductivity in $PrOs_4Sb_{12}$, *J. Phys. Soc. Jpn.* 73(5), 1135 (2004)

29. J. C. Smith, S. Banerjee, V. Pardo, and W. E. Pickett, Dirac point degenerate with massive bands at a topological quantum critical point, *Phys. Rev. Lett.* 106(5), 056401 (2011)

30. G. Kresse and J. Furthmuller, Efficient iterative schemes for ab initio total-energy calculations using a plane-wave basis set, *Phys. Rev. B* 54(16), 11169 (1996)

31. G. Kresse and J. Furthmuller, Efficiency of abinitio total energy calculations for metals and semiconductors using a plane-wave basis set, *Comput. Mater. Sci.* 6(1), 15 (1996)

32. A. Kjekshus, T. Rakke, S. Rundqvist, T. Østvold, A. Bjørseth, and D. L. Powell, Compounds with the skutterudite type crystal structure (III): Structural data for arsenides and antimonides, *Acta Chem. Scand. A* 28a, 99 (1974)

33. There are $n_{\mathrm{Ir}} = 4$ Ir atoms and $n_{\mathrm{Bi}} = 12$ Bi atoms in an $IrBi_3$ primitive cell. At GGA level, $E_{\mathrm{Ir}} = -8.69$ eV for crystalline Ir with space group $FM\overline{3}M$ and $E_{\mathrm{Bi}} = -3.70$ eV for crystalline Bi with space group $IM\overline{3}M$. From Fig. 1(d) we read $E_{\mathrm{IrBi3}} = -82.81$ eV. Substituting the above values in Eq. (1), we arrived at the binding energy $E_b = -3.65$ eV.

34. A. Becke and E. Johnson, A simple effective potential for exchange, *J. Chem. Phys.* 124(22), 221101 (2006)

35. F. Tran and P. Blaha, Accurate band gaps of semiconductors and insulators with a semilocal exchange-correlation potential, *Phys. Rev. Lett.* 102(22), 226401 (2009)

36. W. X. Feng, D. Xiao, Y. Zhang, and Y. G. Yao, Half-Heusler topological insulators: A first principles study with the Tran–Blaha modified Becke–Johnson density functional, *Phys. Rev. B* 82(23), 235121 (2010)

37. D. Doennig, W. E. Pickett, and R. Pentcheva, Confinement-driven transitions between topological and Mott phases in $(LaNiO_3)N/(LaAlO_3)M(111)$ superlattices, *Phys. Rev. B* 89, 12110(R) (2014)

38. J. Werner and F. F. Assaad, Interaction-driven transition between topological states in a Kondo insulator, *Phys. Rev. B* 88(3), 035113 (2013)

39. A. Go, W. Witczak-Krempa, G. S. Jeon, K. Park, and Y. B. Kim, Correlation effects on 3d topological phases: From bulk to boundary, *Phys. Rev. Lett.* 109(6), 066401 (2012)

40. H. M. Weng, J. Z. Zhao, Z. J. Wang, Z. Fang, and X. Dai, Topological crystalline Kondo insulator in mixed valence ytterbium borides, *Phys. Rev. Lett.* 112(1), 016403 (2014)

41. K. Miyamoto, A. Kimura, K. Kuroda, T. Okuda, K. Shimada, H. Namatame, M. Taniguchi, and M. Donath, Spin-polarized Dirac-cone-like surface state with d character at W(110), *Phys. Rev. Lett.* 108(6), 066808 (2012)
42. C. J. Kang, J. Kim, K. Kim, J.-S. Kang, J. D. Denlinger, and B. I. Min, Band symmetries of mixed valence topological insulator: SmB_6, arXiv: 1312.5898 (2013)
43. S. Okamoto, Wenguang Zhu, Y. Nomura, R. Arita, Di Xiao, and N. Nagaosa, Correlation effects in (111) bilayers of perovskite transition-metal oxides, arXiv: 1401.0009 (2014)
44. G. Chen and M. Hermele, Magnetic orders and topological phases from f-d exchange in pyrochlore iridates, *Phys. Rev. B* 86(23), 235129 (2012)
45. Y. H. Chen, H. S. Tao, D. X. Yao, and W. M. Liu, Kondo metal and ferrimagnetic insulator on the triangular Kagome lattice, *Phys. Rev. Lett.* 108(24), 246402 (2012)
46. K. Niwa, D. Nomichi, M. Hasegawa, T. Okada, T. Yagi, and T. Kikegawa, Compression behaviors of binary skutterudite CoP_3 in noble gases up to 40 GPa at room temperature, *Inorg. Chem.* 50(8), 3281 (2011)
47. A. Smalley, M. L. Jespersen, and D. C. Johnson, Synthesis and structural evolution of $RuSb_3$, a new metastable skutterudite compound, *Inorg. Chem.* 43(8), 2486 (2004)
48. T. Caillat, J. P. Fleurial, and A. Borshchevsky, Bridgman-solution crystal growth and characterization of the skutterudite compounds $CoSb_3$ and $RhSb_3$, *J. Cryst. Growth* 166(1–4), 722 (1996)
49. M. Akasaka, T. Iida, G. Sakuragi, S. Furuyama, M. Noda, S. Matsui, M. Ota, H. Suzuki, H. Sato, Y. Takanashi, and S. Sakuragi, Effects of post-annealing on thermoelectric properties of p-type $CoSb_3$ grown by the vertical Bridgman method, *J. Alloys Compd.* 386(1–2), 228 (2005)
50. H. Takizawa, K. Miura, M. Ito, B. Suzuki, and T. Endo, Atom insertion into the CoSb skutterudite host lattice under high pressure, *J. Alloys Compd.* 282(1–2), 79 (1999)
51. X. X. Xi, C. Ma, Z. Liu, Z. Chen, W. Ku, H. Berger, C. Martin, D. B. Tanner, and G. L. Carr, Signatures of a pressure-induced topological quantum phase transition in BiTeI, *Phys. Rev. Lett.* 111(15), 155701 (2013)
52. Y. Nakamoto, H. Sumiya, T. Matsuoka, K. Shimizu, T. Irifune, and Y. Ohishi, Generation of Multi-megabar pressure using nano-polycrystalline diamond anvils, *Jpn. J. Appl. Phys.* 46(25), L640 (2007)
53. J. L. Zhu, J. L. Zhang, P. P. Kong, S. J. Zhang, X. H. Yu, J. L. Zhu, Q. Q. Liu, X. Li, R. C. Yu, R. Ahuja, W. G. Yang, G. Y. Shen, H. K. Mao, H. M. Weng, X. Dai, Z. Fang, Y. S. Zhao, and C. Q. Jin, Superconductivity in topological insulator Sb_2Te_3 induced by pressure, *Scientific Reports* 3, 2016 (2013)
54. J. J. Hamlin, J. R. Jeffries, N. P. Butch, P. Syers, D. A. Zocco, S. T. Weir, Y. K. Vohra, J. Paglione, and M. B. Maple, High pressure transport properties of the topological insulator Bi_2Se_3, *J. Phys.: Condens. Matter* 24(3), 035602 (2012)
55. Y. Q. Li, K. H. Wu, J. R. Shi, and X. C. Xie, Electron transport properties of three-dimensional topological insulators, *Front. Phys.* 7(2), 165 (2012)
56. B. Dóra and R. Moessner, Dynamics of the spin Hall effect in topological insulators and graphene, *Phys. Rev. B* 83(7), 073403 (2011)
57. P. Cheng, C. Song, T. Zhang, Y. Zhang, Y. Wang, J. F. Jia, J. Wang, Y. Wang, B. F. Zhu, X. Chen, X. Ma, K. He, L. Wang, X. Dai, Z. Fang, X. Xie, X. L. Qi, C. X. Liu, S. C. Zhang, and Q. K. Xue, Landau quantization of topological surface states in Bi_2Se_3, *Phys. Rev. Lett.* 105(7), 076801 (2010)
58. C. L. Kane and E. J. Mele, Quantum spin Hall effect in graphene, *Phys. Rev. Lett.* 95(22), 226801 (2005)
59. C. L. Kane and E. J. Mele, Z_2 topological order and the quantum spin Hall effect, *Phys. Rev. Lett.* 95(14), 146802 (2005)
60. K. S. Novoselov, A. K. Geim, S. V. Morozov, D. Jiang, M. I. Katsnelson, I. V. Grigorieva, S. V. Dubonos, and A. A. Firsov, Two-dimensional gas of massless Dirac fermions in graphene, *Nature* 438(7065), 197 (2005)
61. S. Cahangirov, M. Topsakal, E. Aktürk, H. Sahin, and S. Ciraci, Two- and one-dimensional honeycomb structures of silicon and germanium, *Phys. Rev. Lett.* 102(23), 236804 (2009)
62. M. Ezawa, Valley-polarized metals and quantum anomalous Hall effect in silicene, *Phys. Rev. Lett.* 109(5), 055502 (2012)
63. M. Ezawa, A topological insulator and helical zero mode in silicene under an inhomogeneous electric field, *New J. Phys.* 14(3), 033003 (2012)
64. M. Tahir and U. Schwingenschlögl, Valley polarized quantum Hall effect and topological insulator phase transitions in silicene, *Scientific Reports* 3, 1075 (2013)
65. W. F. Tsai, C.Y. Huang, T.R. Chang, H. Lin, H.T. Jeng, and A. Bansil, Gated silicene as a tunable source of nearly 100% spin-polarized electrons, *Nat. Commun.* 4, 1500 (2013)
66. L. Chen, B. J. Feng, and K. H. Wu, Observation of a possible superconducting gap in silicene on Ag(111) surface, *Appl. Phys. Lett.* 102(8), 081602 (2013)
67. M. I. Katsnelson, V. Y. Irkhin, L. Chioncel, A. I. Lichtenstein, and R. A. de Groot, Half-metallic ferromagnets: From band structure to many-body effects, *Rev. Mod. Phys.* 80(2), 315 (2008)
68. D. Xiao, W. Yao, and Q. Niu, Valley-contrasting physics in graphene: Magnetic moment and topological transport, *Phys. Rev. Lett.* 99(23), 236809 (2007)
69. P. E. Blöchl, Projector augmented-wave method, *Phys. Rev. B* 50(24), 17953 (1994)
70. C. C. Liu, H. Jiang, and Y. Yao, Low-energy effective Hamiltonian involving spin-orbit coupling in silicene and two-dimensional germanium and tin, *Phys. Rev. B* 84(19), 195430 (2011)
71. I. V. Solovyev, P. H. Dederichs, and V. I. Anisimov, Corrected atomic limit in the local-density approximation and

the electronic structure of d impurities in Rb, *Phys. Rev. B* 50(23), 16861 (1994)

72. V. I. Anisimov, F. Aryasetiawan, and A. I. Lichtenstein, First-principles calculations of the electronic structure and spectra of strongly correlated systems: The LDA+ U method, *J. Phys.: Condens. Matter* 9(4), 767 (1997)
73. K. T. Chan, J. B. Neaton, and M. L. Cohen, Firstprinciples study of metal adatom adsorption on graphene, *Phys. Rev. B* 77(23), 235430 (2008)
74. J. Ding, Z. Qiao, W. Feng, Y. Yao, and Q. Niu, Engineering quantum anomalous/valley Hall states in graphene via metal-atom adsorption: An ab-initio study, *Phys. Rev. B* 84(19), 195444 (2011)
75. H. M. Weng, T. Ozaki, and K. Terakuta, Theoretical analysis of magnetic coupling in sandwich clusters $V_n(C_6H_6)_{n+1}$, *J. Phys. Soc. Jpn.* 77(1), 014301 (2008)
76. T. O. Wehling, A. V. Balatsky, M. I. Katsnelson, A. I. Lichtenstein, and A. Rosch, Orbitally controlled Kondo effect of Co adatoms on graphene, *Phys. Rev. B* 81(11), 115427 (2010)
77. H. Zhang, C. Lazo, S. Blügel, S. Heinze, and Y. Mokrousov, Electrically tunable quantum anomalous Hall effect in graphene decorated by 5d transition-metal adatoms, *Phys. Rev. Lett.* 108(5), 056802 (2012)
78. Z. H. Qiao, S. A. Yang, W. X. Feng, W.-K. Tse, J. Ding, Y. G. Yao, J. Wang, and Q. Niu, Quantum anomalous Hall effect in graphene from Rashba and exchange effects, *Phys. Rev. B* 82, 161414(R) (2010)
79. D. J. Thouless, M. Kohmoto, M. P. Nightingale, and M. den Nijs, Quantized Hall conductance in a two-Dimensional periodic potential, *Phys. Rev. Lett.* 49(6), 405 (1982)
80. D. Xiao, M. C. Chang, and Q. Niu, Berry phase effects on electronic properties, *Rev. Mod. Phys.* 82(3), 1959 (2010)
81. A. Mostofi, J. R. Yates, Y. S. Lee, I. Souza, D. Vanderbilt, and N. Marzari, Wannier90: A tool for obtaining maximally-localized Wannier functions, *Comput. Phys. Commun.* 178(9), 685 (2008)
82. X. Wang, J. R. Yates, I. Souza, and D. Vanderbilt, *Ab initio* calculation of the anomalous Hall conductivity by Wannier interpolation, *Phys. Rev. B* 74(19), 195118 (2006)